JOURNAL OF MATERIALS SCIENCE, 30 (1995) 4286–4298

On the relationship between microstructure and acoustic emission in Ti–6Al–4V

L. SHAW
Systran Corporation, Dayton, OH 45432, USA
D. MIRACLE
Materials Directorate, Wright-Patterson Air Force Base, Dayton, OH 45433, USA

In situ microstructural observations on slip lines and microfracture processes have been coupled with mechanical deformation to investigate the acoustic emission of Ti–6Al–4V, a two-phase alloy. The material has been subjected to several different heat treatments to produce various microstructures and grain sizes. The dependencies of acoustic emission (AE) characteristics, such as the AE events amplitude, the rate of AE, location of the AE sources and the total events of AE in each deformation test, on work hardening, grain size, second phase content and morphology, and strain rate have been explored. The presence of the second phase, beta, existing in either an intergranular network or thin plates, was found to have little influence on the AE of this material. Furthermore, it was found that the dependencies of the AE characteristics on work hardening, grain size, second phase and strain rate could be explained in terms of the operation of Frank–Read dislocation sources.

1. Introduction

During the last two decades acoustic emission (AE) from composite materials has been utilized to detect initiation and the location of the source of damage, to monitor damage accumulation, to track damage progression, to determine damage severity, and to identify the major failure mechanisms and processes. The attractiveness of the AE technique results from these multiple applications and the fact that results can be obtained in real time. Each of the applications listed above has been extensively investigated on a variety of composite systems including metal–matrix [1–4], ceramic–matrix [5–7], and polymer–matrix [8–12] composites with varying success. Among these applications, the identification of specific failure mechanisms and processes has been the most challenging task in the application of the AE technique. The complexity in this area is due to the fact that many damage mechanisms (e.g. plastic deformation of matrices, matrix cracking, matrix twinning, interfacial debonding, interfacial friction, delamination, fibre breakage, etc.) cause AE and may occur simultaneously. This is further complicated by similar AE characteristics for some different damage processes and by the anisotropic properties of composites. Notwithstanding these difficulties, several attempts have recently been made to identify mechanisms of AE in composite materials [1, 11, 13, 14]. For example, using *in-situ* AE monitoring with simultaneous scanning electron microscope recording, Siegmann and Kander [13] have divided AE amplitude distribution of a polymer-based composite into three ranges corresponding to matrix damage, fibre–matrix debonding and fibre breakage. Working with replicates and a closed-circuit television system for *in-situ* monitoring of the damage evolution, Bakuckas *et al.* [1] attempted to relate AE to the failure mechanisms in titanium β21S–SiC composites and suggested that direct correlations between damage mechanisms (i.e. matrix plastic deformation, matrix cracking, fibre-matrix debonding, cracking of brittle reaction zone and fibre breakage) and AE events amplitude do exist in this composite system. Despite these efforts, the identification of the major failure mechanisms and processes through the AE technique is still in its early stage of development.

Obviously, one approach to establish the correspondence between AE events and composite failure mechanisms is to diagnose the composites by investigating the AE characteristics of matrices alone, comparing these with the AE response from model composites such as single-fibre composites, and finally addressing real composites. The first two phases are necessary for establishing the basic response characteristics for prediction of the acoustic response from the real composites. Hence, a program containing these three phases aimed at monitoring the damage progression in Ti-based continuous-fibre reinforced composites using AE technique has been developed. Such a three-phase program is necessary, especially for metal–matrix composites because AE during the deformation of metals alone could be quite complicated. Sources of AE during the deformation of metals include moving dislocations, twinning, grain boundary sliding, the fracture and decohesion of inclusions, intergranular microfracture, cleavage microfracture,

0022–2461

and microvoid coalescence [15]. Because of the complexity of matrix deformation alone, this study, as the first phase of the program, reports only the AE response of Ti–6AI–4V matrix (a two-phase alloy) with various processing conditions and microstructures at a fixed composition.

2. Experimental procedure

Ti–6A1–4V sheets with a thickness of 1.524 mm (0.06 inch) were supplied by RMI Titanium. The as-received sheets were in an annealed condition (i.e. hot rolled starting at 927 °C, annealed at 730 °C for 4 h and furnace-cooled). The sheets received were first cut, using an electro-discharge machine, into dog-bone shaped tensile specimens with a gauge length of 22 or 28 mm, and then subjected to heat treatment to examine the microstructure effect on the AE of this material. The heat treatment temperatures and cooling rates were selected in such a way that various grain sizes and second-phase morphologies could be obtained and evaluated. The heat treatment was conducted using a box-type furnace. The specimens, which were wrapped with tantalum foil and encapsulated in quartz tubes with back-filled argon, were subject to one of the following heat treatments: (a) annealed at 925 °C for 1.5 h and furnace-cooled to room temperature (with a cooling rate of ca. 8 °C min^{-1}); (b) 960 °C for 1.5 h and furnace-cooled; (c) 1010 °C for 1.5 h and furnace-cooled; and (d) 1100 °C for 1.0 h, cooled to 700 °C at 2 °C min^{-1}, and then furnace-cooled to room temperature. In order to avoid acoustic noise from any oxide layer on the surface of the dog-bone specimens, each specimen, after heat treatment, was ground with SiC abrasive paper to 320 grit and cleaned with acetone. Some specimens were further polished to 1 μm diamond paste and then electropolished in an electrolyte (6% perchloric acid in a mixture of methanol and 2-butanol) with a 20 V d.c. at − 50 °C for 30 min. The polished surface allowed *in situ* optical observation of the slip lines and various microfracture processes during tensile tests.

Tensile tests were performed using a servo-hydraulic machine at ambient temperatures. The tests were displacement controlled with a nominal strain rate of 2.9×10^{-3}, 2.9×10^{-4} or 3.8×10^{-5} s^{-1}. A knife-edge extensometer was mounted to monitor the strain within the gauge as a function of load throughout the test. In order to relate the microscopic damage of the tested materials to AE, some tensile tests were conducted using a micro-straining stage built in this laboratory. This micro-straining stage allows *in situ* observation of the slip lines and various microfracture processes during testing with an optical microscope.

AE was monitored using an AE Data Acquisition System. Care was taken to standardize all experimental procedures so that valid comparisons could be made between different tests. Two piezoelectric transducers, sensitive to acoustic signals with frequencies from 10 KHz to 1 MHz, were attached to the shoulders of the specimens by a thin layer of vacuum grease, under a constant pressure applied by a rubber band. The output signals from the sensors were amplified by pre-amplifiers with a gain of 40 dB and a 100–400 KHz bandpass filter. The post-amplifier gain was 20 dB and the hit definition time used to distinguish between separate events was set to 200 μm for the dimension of the present specimens. After the installation of the transducers, a pencil lead break procedure (ASTM E976) was used for AE location calibration. A mechanical pencil with a 0.5 mm diameter 2H lead was used and the lead was broken at three locations within the gauge length of the specimen with one location near sensor 1, another near sensor 2 and the last one at the centre of the specimen. The location of AE events with the origin designated at sensor 1 was calculated as follows:

$$x = (L + \Delta t\, V)/2 \qquad (1)$$

where L is the distance between the two sensors, $\Delta t = t_1 - t_2$ with t_1 and t_2 being the arrival time of sensors 1 and 2, respectively, and V is the acoustic velocity.

Several precautions were taken to avoid extraneous acoustic noise. First, the amplitude threshold was set at 45 dB, which was found to be very effective in limiting the acoustic noise because most of the noise had amplitudes < 45 dB. Second, the spatial filtering of AE events through post-test data reduction was performed to exclude the AE from outside the gauge

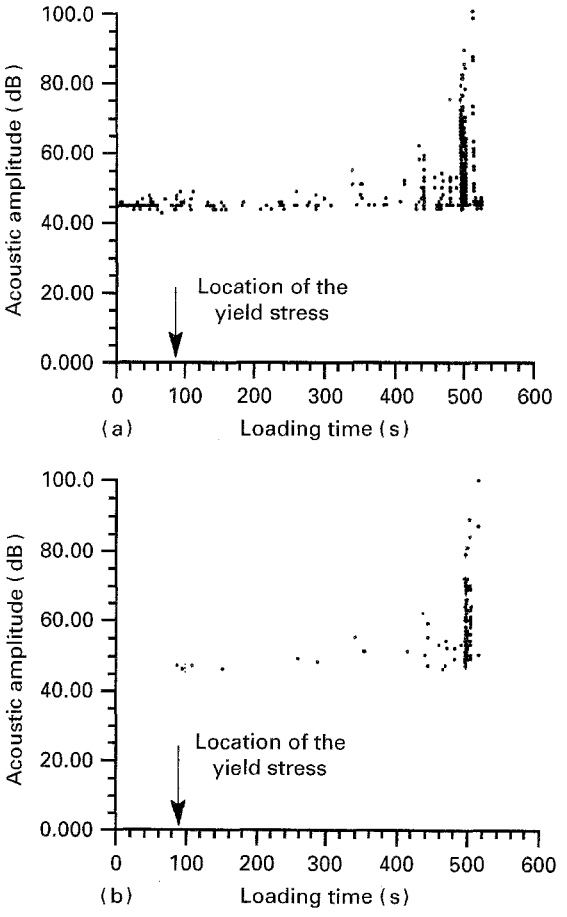

Figure 1 The extension dependence of the amplitude of discrete AE events during tensile deformation of a Ti–6Al–4V sheet annealed at 730 °C and furnace-cooled. (a) AE before the filtering and (b) AE after the filtering of the unpaired AE events and AE events outside the gauge length and from the middle of the two transducers. (Strain rate: 2.9×10^{-4} s^{-1}.)

length and precisely at the middle of the two transducers. AE from outside the gauge length may come from computer terminals, the hydraulic servo valve, motors and slip of the specimen relative to the grips. AE precisely at the middle of the two transducers may be due to electronic noise spikes which essentially appeared simultaneously on both transducers. Thus, eliminating simultaneous triggers eliminated electronic noise spikes, although valid AE from the specimens precisely at the middle of the two transducers were also eliminated. Finally, unpaired acoustic events were filtered out from the final data. It was found that before any loading AE was detected only by the transducer close to the grip which was directly connected to the driving shaft of the motor, while the other transducer exhibited no acoustic emission. This phenomenon was not clearly understood. However, this was very likely due to the attenuation of the specimens. The effect of these precautions is clearly seen in Fig. 1, which shows the extension dependence of the amplitude of discrete AE events before and after the elimination of unpaired AE events and AE events outside the gauge length and from the middle of the two transducers. Thus, unless noted, all AE events detected have been screened through the spatial filtering and unpaired-event filtering, and only AE events within the gauge length will be presented in the following text.

3. Results and discussion

3.1. Microstructure

Microstructures of Ti–6Al–4V for the as-received and heat treated conditions are presented in Fig. 2; the cross-sections shown in the figure are all perpendicular to the travel direction of the hot rolling. In the as-received condition (i.e. annealed at 730 °C), the microstructure consisted of elongated alpha grains (grey) and intergranular beta (light). The average alpha grain size was 3 μm along the short axis and 10 μm along the long axis. After annealing at 925 °C, the alpha phase (grey) became less elongated with an average grain size of 7 μm along the short axis and 10 μm along the long axis. Meanwhile, beta phase (light) became more continuous along the grain boundaries of the alpha phase. As the annealing temperature increased to 960 °C, the alpha phase (grey) became more or less equiaxed with an average grain size of 10 μm. At this temperature, the beta phase (light) became almost continuous along the grain boundary of the alpha phase. When the alloy was annealed above the beta transus temperature, a substantial change in microstructure was observed. For the condition of annealed at 1010 °C and furnace-cooled to room temperature, a typical Widmanstatten alpha resulted. The width of the alpha plates (grey) was typically ca. 2 μm with thin beta plates (light being < 0.5 μm. The prior beta grain size outlined by the alpha that was first to transform (Fig. 3) was ca. 250 μm. As can be seen from Fig. 3, in some prior beta grains the alpha plates formed along one set of preferred crystallographic planes of the prior beta matrix, while in the other prior beta grains the alpha plates formed along several sets of planes. As such, Widmanstatten colonies generally had a smaller size than the prior beta grains and their average size was ca. 150 μm. When the annealing temperature was further increased to 1100 °C and cooled with a very slow cooling rate (i.e. 2 °C min^{-1}), both alpha and beta plates became coarser. Under this condition, the alpha plates had a typical width of 7 μm, while beta plates were typically 1 μm wide. The prior beta grain size became ca. 500 μm with an average Widmanstatten colony size of 200 μm.

3.2. Effect of work hardening

The microstructural change and stress–strain curve during tensile deformation of Ti–6A1–4V sheet annealed at 730 °C is shown in Fig. 4. The letters along the stress–strain curve indicate the locations at which the test was interrupted to take micrographs. The load in these micrographs was applied vertically. Note that the orientation of the tensile stress axis was coincidentally in such a direction that it was almost parallel to

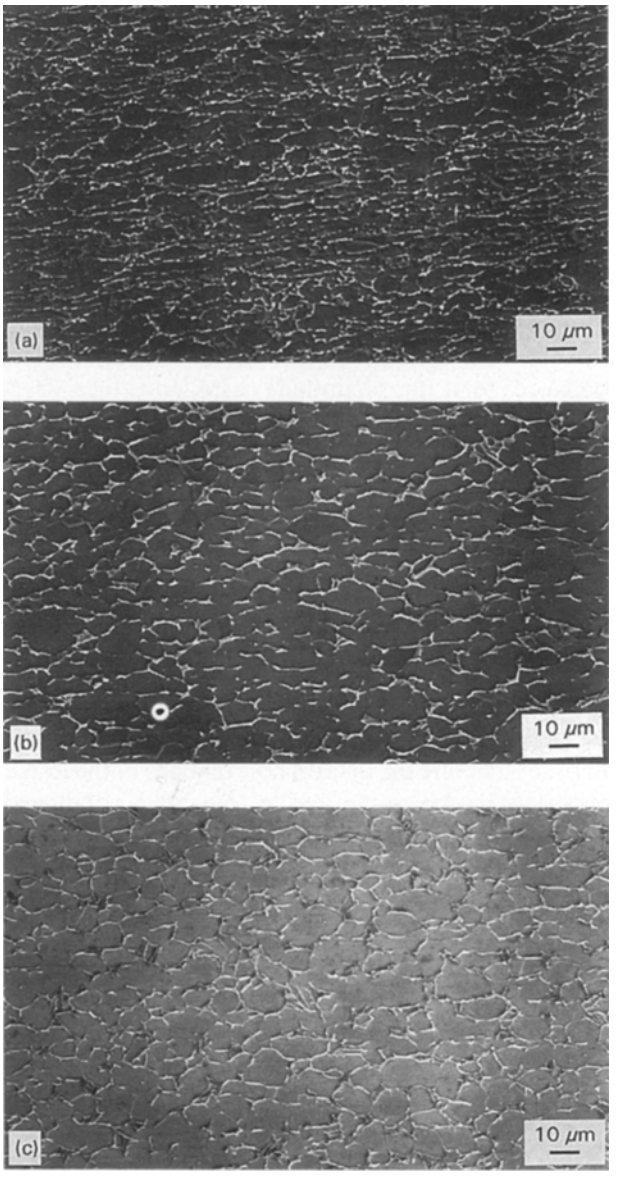

Fig. 2 (Continued)

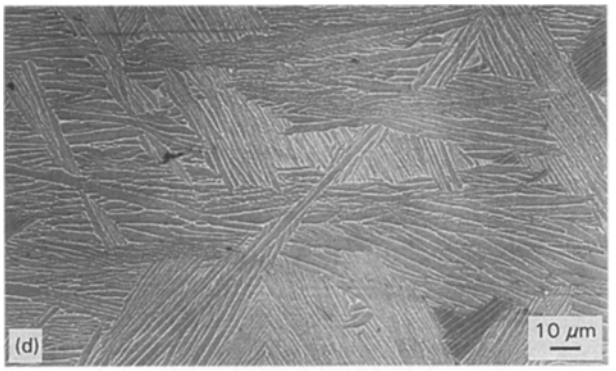

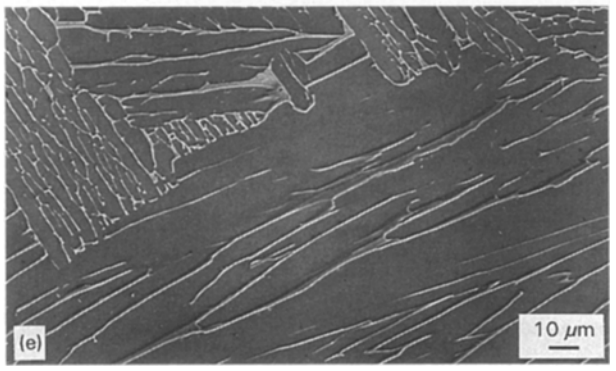

Figure 2 Secondary electron images of Ti–6Al–4V microstructures: (a) annealed at 730 °C and furnace-cooled; (b) annealed at 925 °C and furnace-cooled; (c) annealed at 960 °C and furnace-cooled; (d) annealed at 1010 °C and furnace-cooled; (e) annealed at 1100 °C, cooled to 700 °C at 2°C min^{-1} and then furnace-cooled.

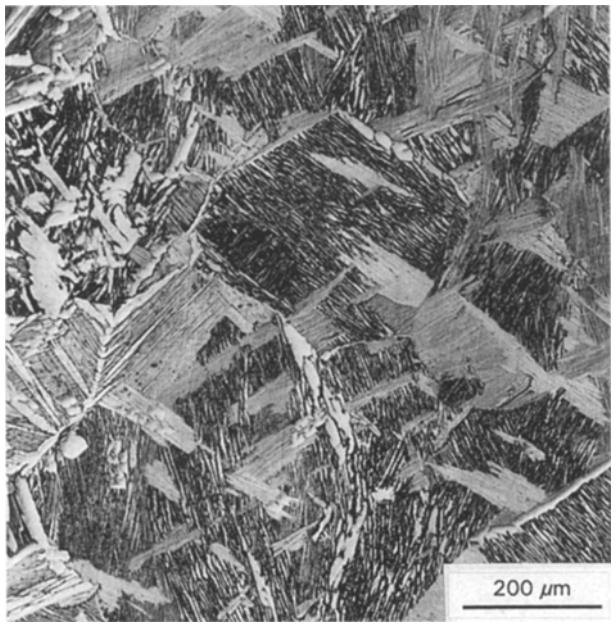

Figure 3 Optical microstructure of Ti–6Al–4V annealed at 1010 °C for 1.5 h and furnace-cooled, showing the prior beta grain boundaries.

the long axis of the elongated alpha phases for all the tests. From point A–C, the surface of the specimen looked the same as shown in Fig. 4b. When point D was reached, some slip lines were observed, as indicated by the arrows in Fig. 4c. As plastic deformation continued, more and more slip lines were observed, as indicated in Fig. 4d and e. It is noted that most of the slip lines were oriented at an angle ranging from 40 to 80° with respect to the tensile axis. Furthermore, these slip lines did not cross alpha grain boundaries, suggesting that the grain boundary is an effective barrier to dislocation motion. Since the average alpha grain size was 3 μm perpendicular to the tensile axis and 10 μm along the tensile axis, the alpha grains behaved as 3 μm grains in terms of being a barrier to dislocation motion. The phenomenon that slip lines did not cross the alpha grain boundary has also been observed in other specimens which had a microstructure of elongated or equiaxed alpha with intergranular beta, as shown in Fig. 5.

A typical acoustic response and the corresponding stress–strain curve of Ti–6A1–4V sheets annealed at 925 °C for 1.5 h are shown in Fig. 6. Note that because AE recording started synchronously with tensile testing, there is a direct relation between the strain and loading time. Several features about AE events can be seen from this figure. First, no AE events were detected during elastic deformation. Second, AE events started being detected before and near the yield stress, which is defined in this text as the yield strength with 0.2% plastic deformation. Third, the amplitude of AE events rose sharply to a maximum near the yield stress, and then decreased gradually as the plastic strain increased. Fourth, after a certain amount of plastic strain the acoustic events amplitude fell below the threshold (45 dB), leading to no detectable AE events. Fifth, the acoustic event's amplitude suddenly increased just before final fracture.

The acoustic response exhibited by the specimens annealed to 925 °C can be explained in terms of dislocation motion. It is commonly accepted that the sudden strain increment that results from the unpinning of dislocations or from the activation of dislocation sources can result in observable AE [16–26]. By applying elastodynamic theory, Scruby *et al.* [19, 20] has obtained a formula describing the peak normal surface displacement beneath the transducer, u, due to the expansion of a glissile dislocation loop from starting radius of zero to a final radius (r), i.e.:

$$u = Br\dot{r} \tag{2}$$

where u is the peak normal surface displacement, $\dot{r}$ is the velocity at which the dislocation loop expands, and B is a coefficient related to the shear and longitudinal wave speeds, depth of the dislocation source and Burger's vector of the dislocation loop. For an AE due to the expansion of a dislocation loop to be detected, the peak normal surface displacement should be larger than the displacement sensitivity of a transducer (e.g. 10^{-14} m). It is clear from Equation 2 that the displacement amplitude is proportional to the distance of dislocation propagation, and to the velocity at which it moves. Furthermore, if large numbers of dislocations are closely spaced and move synchronously, their emitted wave fields add. In this case, the peak normal surface displacement becomes:

$$u = nBr\dot{r} \tag{3}$$

where n is the number of moving dislocations. Based on this simple model, the present measurements can

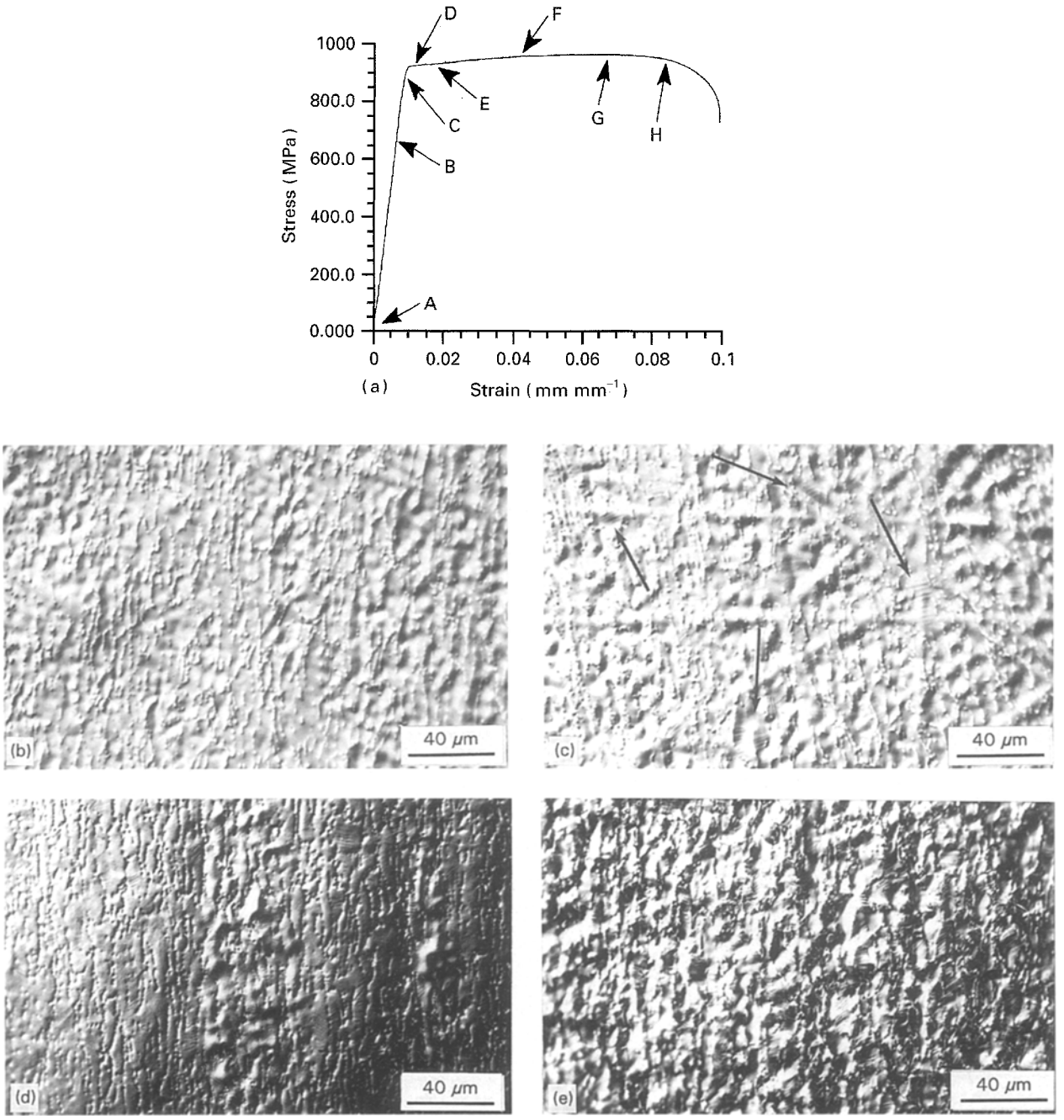

Figure 4 The microstructural change and stress–strain curve during tensile deformation of Ti–6Al–4V sheet annealed at 730 °C. The letters along the stress–strain curve in (a) indicate the locations at which the test was interrupted to take micrographs. The optical images of the specimen surface corresponding to points C, D, F and G are shown in (b), (c), (d) and (e), respectively.

be explained as follows. The few AE observed before and near the yield stress can be attributed to micro-yielding of the specimen. At the yield stress, many closely-spaced dislocation sources (such as Frank–Read sources) are activated synchronously, generating a large number of dislocations. Many of these dislocations can move a distance of about a grain size at this stage, therefore producing many high amplitude AE (large n and r in Equation 2). As plastic deformation proceeds, work hardening reduces the mean free path of moving dislocations, leading to AE events with lower amplitudes (smaller r in Equation 2). After a certain amount of plastic strain the mean free path is so small that the acoustic events amplitude falls below the threshold (45 dB), resulting in few events being detected. Near the final fracture, the acoustic events amplitude suddenly increases because of microvoid coalescence and shear fracture. A similar explanation of the strain dependence of the AE events amplitude has also been proposed in Ref. 15.

The operation of Frank–Read sources as a source of AE can also be examined from the strain dependence of AE events frequency and the rate of AE (i.e. the number of AE events per unit time). As the deformation increases, AE signals are expected to become richer in high frequency components because of the reduction of the mean free path between sessile dislocations, which therefore decreases the lifetime of the sources [17, 27]. However, our current sensors did not allow for frequency analysis because of their narrow band characteristics. Nevertheless, the analysis of the

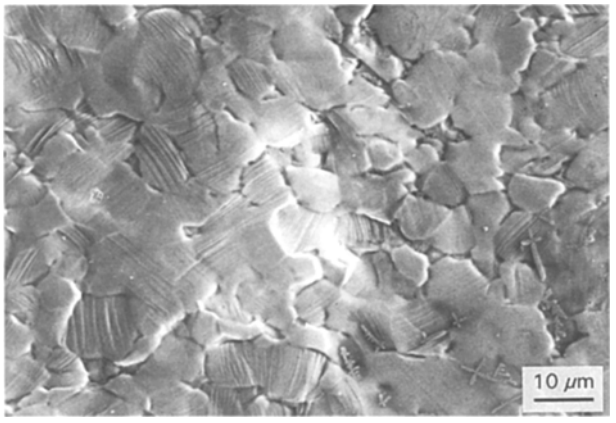

Figure 5 Secondary electron image of a Ti–6Al–4V specimen annealed at 925 °C and deformed with 6% strain.

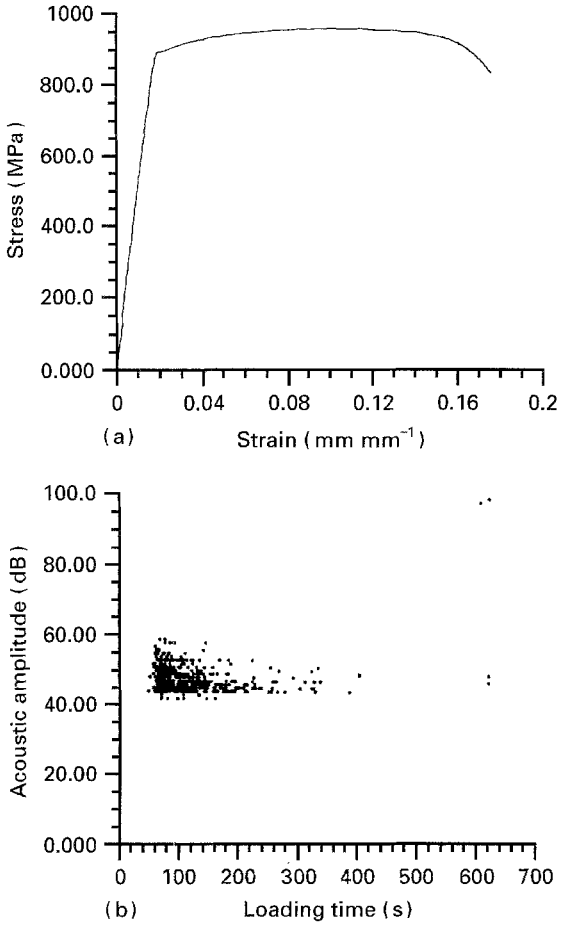

Figure 6 The extension dependence of the stress and the amplitude of discrete acoustic emission events during tensile deformation of a Ti–6Al–4V sheet annealed at 925 °C for 1.5 h and furnace-cooled. (Strain rate: $2.9 \times 10^{-4}\,s^{-1}$.)

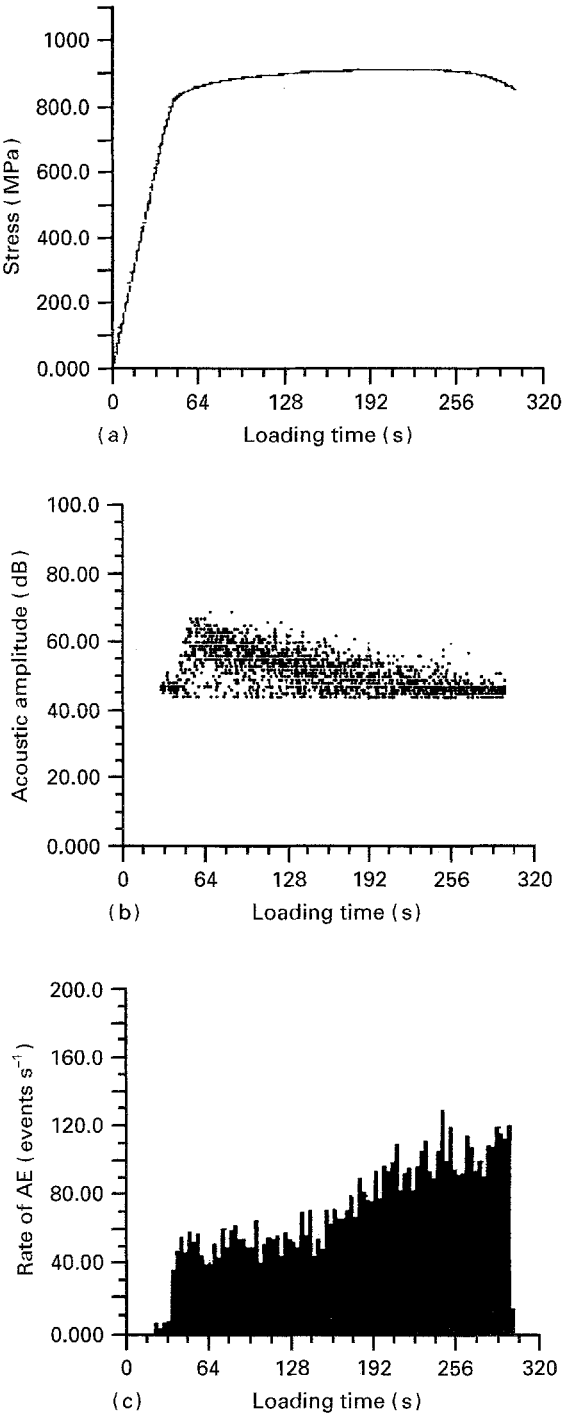

Figure 7 The extension dependency of (a) the stress, (b) the amplitude of AE and (c) the rate of AE per unit time for a specimen annealed at 960 °C and deformed at a strain rate of $2.9 \times 10^{-4}\,s^{-1}$.

rate of emission did provide insights into the strain dependence of dislocation motion. Fig. 7 shows the rate of emission as a function of the loading time along with the corresponding stress–strain curve and the curve of the AE events amplitude for a Ti–6A1–4V specimen annealed at 960 °C. Note that the AE events amplitude for the specimens with this processing condition behaved like those annealed at 925 °C (Fig. 6), i.e., near the yield stress AE events amplitude exhibited a maximum, and it then decreased gradually as the material work hardened. The rate of emission was found to increase sharply near the yield stress and continue to increase gradually as the material work hardened. An explanation of this phenomenon can be suggested in terms of the decrease of the mean free path with the increase of the plastic deformation. A decrease in the mean free path requires the activation of more dislocation sources to keep up with the externally applied constant displacement rate. As such, as the material work hardens, more AE events occur.

The increase of the rate of emission with work hardening was also observed in the specimens annealed at 1010 °C. However, the specimens annealed at 925 °C exhibited the opposite trend, i.e. the rate of

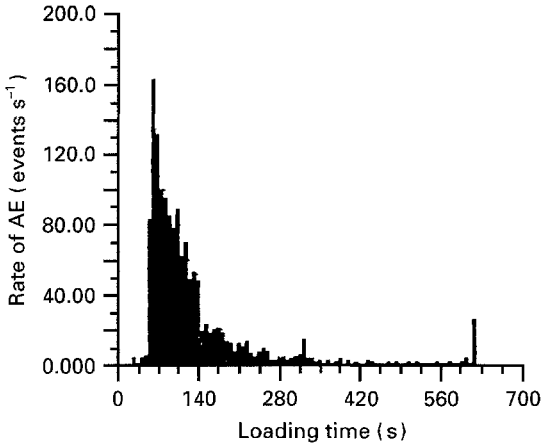

Figure 8 The extension dependency of the rate of acoustic emission of the specimen shown in Fig. 6.

emission decreased as plastic deformation increased (Fig. 8). The discrepancy can be explained as follows. As plastic deformation increased, more dislocation sources were activated to compensate the reduction of the mean free path, but each of the dislocation loops expanded a smaller distance. As such, more AE events with lower amplitudes resulted. For the specimens annealed at 960 °C and 1010 °C, their starting AE events' amplitudes near the yield stress were high, and their amplitudes were still high enough to pass the threshold even though some decrease in the amplitude occurred with work hardening. Therefore, more AE events with lower amplitudes were detected as plastic deformation increased. In contrast, the specimens annealed at 925 °C had low AE events amplitudes near the yield stress. As the material work hardened, the AE events amplitudes became even lower and fell below the threshold. Thus, even though more AE events occurred with the increase of work hardening, less events were detected due to their low amplitudes.

Finally, it should be pointed out that the rate of AE near the yield stress for the specimens annealed at 925 °C was higher than those annealed at 960 °C, as shown in Figs 7 and 8. This is believed to be a reflection of the fact that small grained specimens have to activate more dislocation sources than large grained specimens to compensate for their shorter mean free path at the beginning of plastic deformation.

3.3. Location of AE sources

The deformation process of Ti–6A1–4V can be better understood if the AE event's amplitude and arrival time are plotted against the location of AE events. Two sets of these curves corresponding to the specimens in Figs 1 and 6 are shown in Figs 9 and 10, respectively. Because the loading time of the tensile tests was also the arrival time for AE events, the relation between Figs 1 and 9 and Figs 6 and 10 can be found based on the time scale. Fig. 9a suggests that yielding occurred first at the location near sensor 1 and then spread out towards the location near sensor 2. Fig. 9b shows that the location of the final fracture was near sensor 1 because high amplitude AE

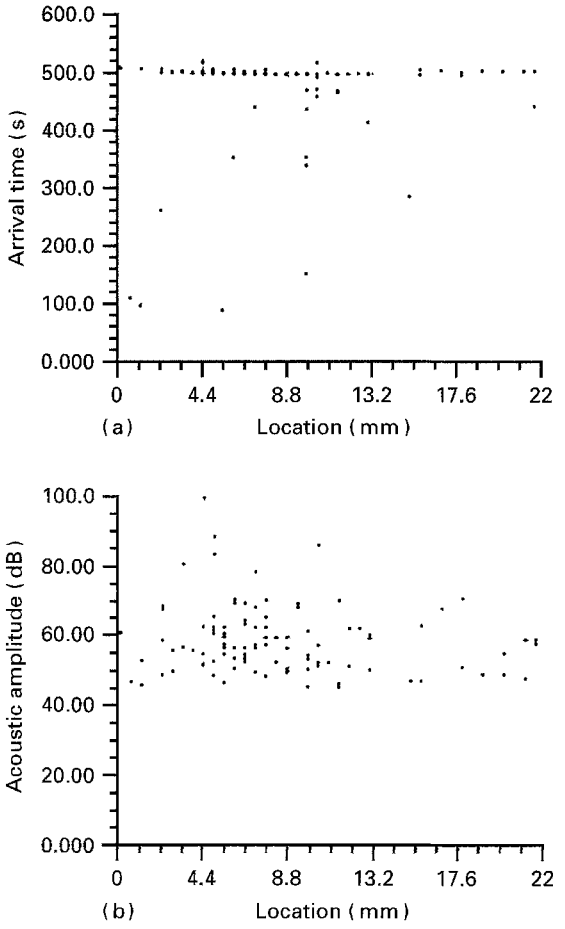

Figure 9 (a) The arrival time and (b) the amplitude of AE events as a function of the spatial location within the gauge length of a specimen annealed at 730 °C and furnace-cooled. The origin of the position is set at one end of the gauge length and is next to sensor 1.

events (> 98 dB) occurred near sensor 1. Similar inference can also be made from Fig. 10, i.e. yielding occurred first at the location near sensor 1 and the final fracture was also located near sensor 1. These inferences are in agreement with the common observation that yield occurs at certain locations within the gauge length and spreads out to the whole specimen [26]. The current results also suggest that a weak cross-section in Ti–6A1–4V is usually the location where yielding occurs, and where fracture initiates.

Although the accuracy to locate the AE sources was calibrated to be within $\pm$ 2 mm before each test, the final fracture location could be detected away from the real position by $\pm$ 5 mm (e.g. Figs 1, 6, 9 and 10) or in the worst case the AE signals from the final fracture were not paired in the two sensors (e.g. Fig. 7 in which there are no AE events with amplitudes > 98 dB right before the fracture). This was caused by the instant separation of the specimen into two parts. Thus, at the moment of the final fracture the two sensors were connected to two pieces of the specimen. Nevertheless, the experimental results in the present study indicated that either the AE signals of the final fracture were unpaired or they were detected within $\pm$ 5 mm from the real fracture location. As such, the conclusion made above regarding the location of the final fracture is valid.

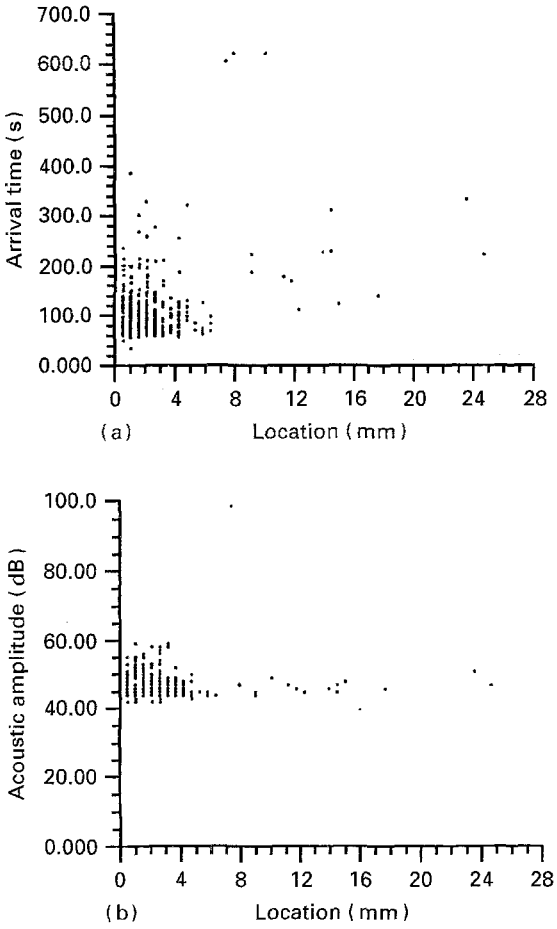

Figure 10 (a) The arrival time and (b) the amplitude of AE events as a function of the spatial location within the gauge length of a specimen annealed at 925 °C and furnace-cooled. The origin of the position is set at one end of the gauge length and is next to sensor 1.

3.4. Strain rate dependence

The effect of strain rate on the acoustic response is shown in Fig. 11, where the specimens annealed at 1010 °C were deformed at a nominal strain rate of 2.9×10^{-3}, 2.9×10^{-4} and 3.8×10^{-5} s^{-1}. It is obvious that the AE event's amplitude near the yield stress increases with strain rate. The strain rate dependence of the maximum AE events amplitude near the yield stress, the rate of emission near the yield stress and the total AE events in each test are summarized in Table I. Also included are the mechanical data and the data from the specimens annealed at 730 °C, which were the other set of specimens subject to deformation with different strain rates. Only a few discrete AE events were detected for the specimens annealed at 730 °C at three deformation rates. Thus, the comparisons between the rates of emission near the yield stress and between the total AE events in this sample series were not reported in the table. Nevertheless, the data clearly indicate that the rate of emission near the yield stress increased with strain rate for the specimens annealed at 1010 °C. Furthermore, it is noted that the maximum AE events amplitude near the yield stress increases with strain rate for both sets of the specimens tested. Similar phenomena have also been observed with aluminium, aluminium alloys, copper, copper alloys, magnesium and iron [21, 27, 28]. It is believed that the increase of the AE events amplitude with

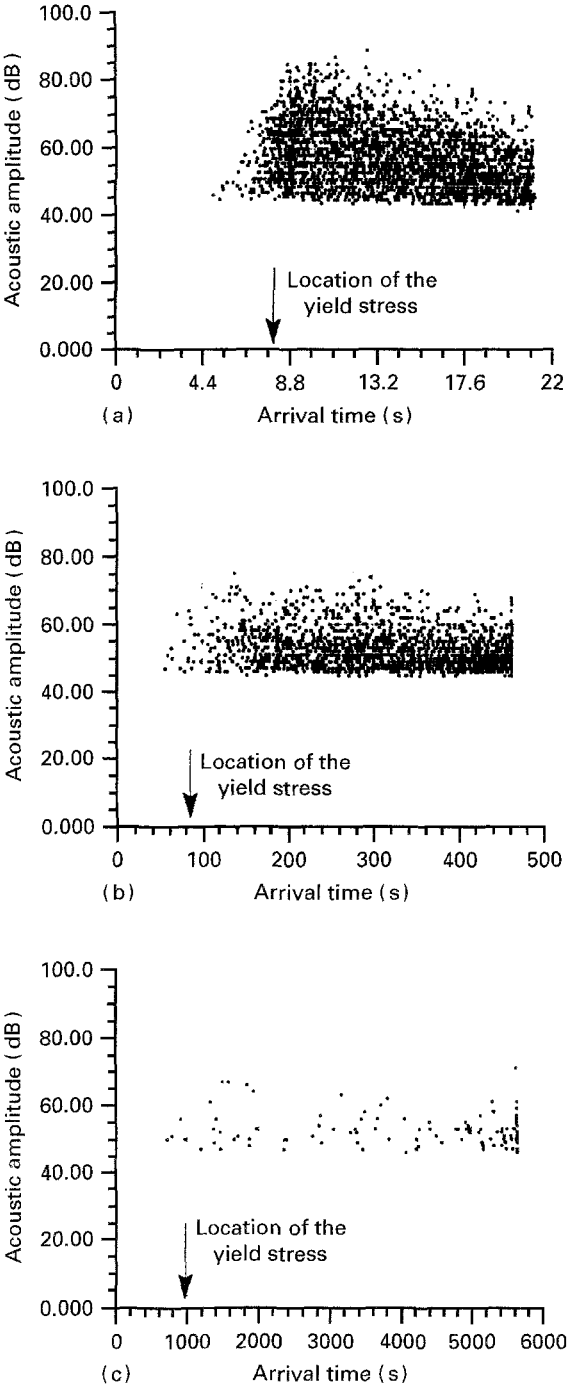

Figure 11 The strain rate dependency of the acoustic response for the specimens annealed at 1010 °C and furnace-cooled. (a) Deformed at a nominal strain rate of $2.9 \times 10^{-3} s^{-1}$; (b) deformed at $2.9 \times 10^{-4} s^{-1}$; and (c) deformed at $3.8 \times 10^{-5} s^{-1}$.

strain rate is due to the increase in the population of moving dislocations and/or in the velocity of moving dislocations (n and/or $\dot{r}$ increases in Equation 2) in order to keep up with high strain rates. The increase in the rate of emission with strain rate has been attributed to a greater frequency of mechanism operation rather than the change of the mechanism [20].

It is interesting to note that the total AE events in each test are almost the same for the specimens tested at a strain rate of 2.9×10^{-3} and $2.9 \times 10^{-4} s^{-1}$. This result indicates that although high strain rates increase the rate of AE, the total AE events do not increase. The fact that the specimen tested at $3.8 \times 10^{-5} s^{-1}$ did not follow this pattern was

TABLE I Strain rate dependency of AE and mechanical properties with Ti–6Al–4V

Strain rate (s^{-1})	Ti–6Al–4V annealed at 1010 °C					Ti–6Al–4V annealed at 730 °C
	Maximum AE amplitude near the yield stress (dB)	Rate of emission near the yield stress (events s^{-1})	Total AE events	Elongation (%)	Tensile strength (MPa)	Maximum AE amplitude near the yield stress (dB)
3.8×10^{-5}	68	ca. 3	ca. 170	32	980	No AE
2.9×10^{-4}	75	ca. 10	ca. 2320	24	1000	47
2.9×10^{-3}	88	ca. 300	ca. 2350	20	1020	60

TABLE II Acoustic response of Ti–6Al–4V with different heat treatments (strain rate = 2.9×10^{-4} s^{-1})

Heat treatment condition	Effective grain size (μm)	Maximum AE amplitude near the yield stress (dB)	Total AE events	Rate of emission near the yield stress (events s^{-1})
Annealed at 730 °C	3	47	ca. 30	Near zero
Annealed at 925 °C	7	60	ca. 720	ca. 160
Annealed at 960 °C	10	68	ca. 1680	ca. 50
Annealed at 1010 °C	150	75	ca. 2320	ca. 10
Annealed at 1100 °C	200	No AE near the yield stress	ca. 425	0

probably due to its non-detectable AE events which had low amplitudes. Nevertheless, the results from strain rates of 2.9×10^{-3} and 2.9×10^{-4} s^{-1} suggest that in this strain rate range the AE mechanisms do not change. The difference between these two rates is the high rate of emission over a short period of time versus the lower rate of emission over a longer period of time.

3.5. Grain size effect

The effects of grain size on AE are summarized in Table II. The grain sizes listed in the table are the effective grain sizes, i.e. the dimensions which acted as barriers to dislocation motion in the present tensile tests. For example, it is shown in Fig. 4 that although the specimen annealed at 730 °C had elongated alpha grains with 3 μm along the short axis and 10 μm along the long axis, the alpha grains behaved like 3 μm in size in terms of being a barrier to dislocation motion. Specimens annealed at 1010 and 1100 °C had Widmanstatten microstructures. However, *in situ* microstructural observation during tensile tests showed that slip lines crossed alpha and beta phases within individual colonies rather than being limited in an alpha or beta phase (Fig. 12) . Thus, for the specimens with Widmanstatten microstructure, the effective grain size was considered to be the size of their Widmanstatten colonies. It can be seen from Table II that the current set of specimens, except for the specimens annealed at 1100 °C, showed several general trends: (a) the maximum AE events amplitude near the yield stress increased with grain size; (b) the total events of AE in each test increased with grain size; and (c) the rate of emission near the yield strength decreased with grain

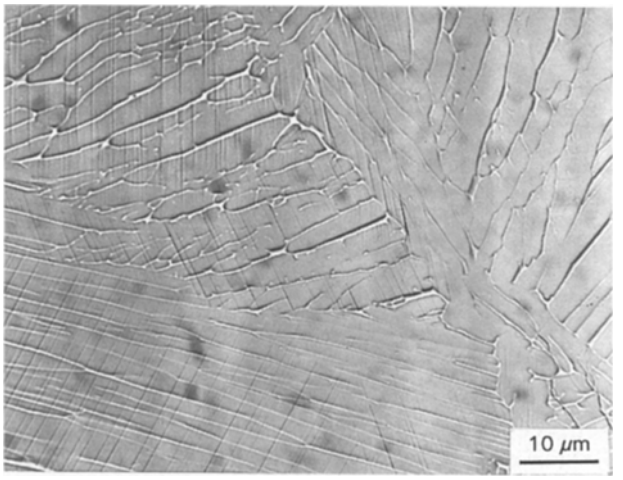

Figure 12 Secondary electron image of a specimen annealed at 1010 °C and deformed with a strain of 4%.

size. The specimens annealed at 730 °C did not exhibit the highest rate of emission near the yield strength, and this is believed to be due to their low amplitude AE. The exception of the specimens annealed at 1100 °C was found to be related to a change of the deformation mechanism, which will be discussed in the next section.

Some investigators have also found that AE power increases with grain size [20], while others have found that AE power increases first and then decreases with increasing grain size [16, 18, 20]. Despite this discrepancy, the current results can be explained solely in terms of the operation of Frank–Read sources. Increasing grain size increases the largest radius the dislocation sources can expand, and therefore increases the maximum amplitude of AE near the yield

stress. Large grained specimens have more detectable AE because of the high amplitude of these AE. Thus, the total events of AE in each test increases with increasing grain size. The longer distance for the dislocation sources to expand in the large grain specimens would lead to a lower frequency of mechanism operation for an externally constant strain rate. As a result, at the constant strain rate and specimen volume the rate of emission near the yield stress would decrease with increasing grain size.

3.6. Plastic deformation versus cracking and fracture

Fracture surfaces of the specimens with different heat treatments are shown in Fig. 13. The dimple appearance of the specimens annealed at 925 and 1010 °C suggests that these specimens had a ductile fracture. The specimens annealed at 730 and 960 °C also exhibited fracture surfaces with dimple characteristics. Recall that specimens annealed at 1010 °C had a Widmanstatten microstructure, while the other three heat treatment conditions (730, 925 and 960 °C annealing) gave microstructure of elongated or equiaxed alpha plus intergranular beta. Nevertheless, the final fracture of these specimens involved a similar mechanism, i.e. microvoid coalescence. It is, therefore, concluded that the sudden increase of AE just before the final fracture in different specimens was due to microvoid coalescence. The amplitude of AE due to this process varied from specimen to specimen, and ranged from 45 to 90 dB without including the final fracture which usually had an amplitude of 99 dB. No clear rules have yet been found to govern the amplitude of AE from microvoid coalescence. However, the current results indicate that Ti–6Al–4V, a material with high yield strength and limited work hardening capacity, could produce high amplitude AE during microvoid coalescence; this is in agreement with other studies [15]. As summarized in Ref. 15, materials with low yield strength and high work hardening capacity do not usually produce detectable AE because the decrease in net load supporting area is balanced by the increased flow stress of the deforming intervoid ligament. In contrast, for materials with high yield strength and limited work hardening capacity, microvoid coalescence proceeds by an alternating shear coalescence because the loss of load supporting area cannot be compensated by work hardening. Thus, these materials are likely to produce detectable AE.

The fracture of the specimens annealed at 1100 °C exhibited a quasi-cleavage appearance. The crack propagation paths could not be clearly deduced from the fracture surface. However, *in situ* microstructural observation during tensile tests suggested that some of the microcracks propagated along the alpha–beta interface, while others propagated along the colony boundary or cut though the alpha and beta phases within individual colonies. Accompanied with the change of fracture surface, the acoustic response of these specimens was also changed. A typical stress–strain curve and acoustic response from these specimens are shown in Fig. 14. It can be seen that near the yield stress there was no AE and that it was only detected after ca. 3% strain. The *in situ*

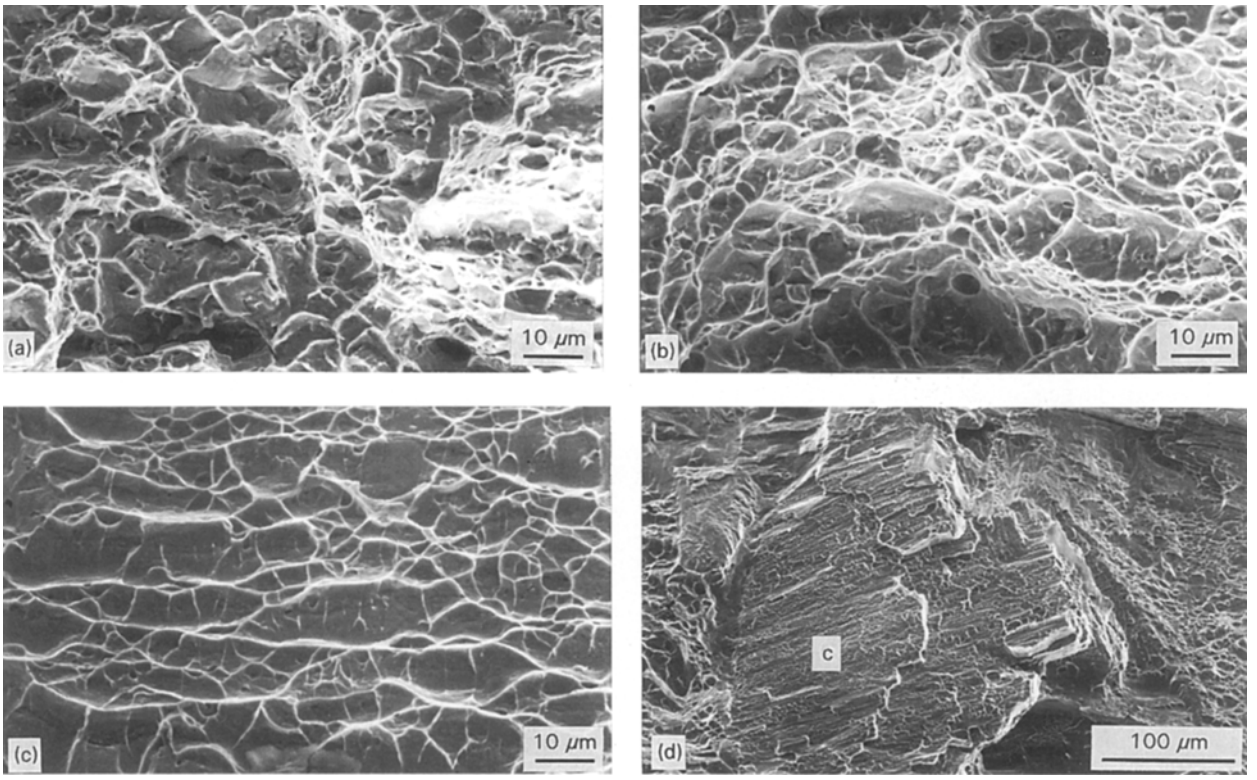

Figure 13 Fracture surfaces of the specimens with a condition of (a) annealed at 925 °C and furnace-cooled; (b) annealed at 1010 °C and furnace-cooled; (c) annealed at 1100 °C and cooled at a speed of 2 °C min^{-1}; and (d) the same processing conditions as (c), but a lower magnification to show the overall fracture surface. The letter "c" indicates the location where (c) was taken.

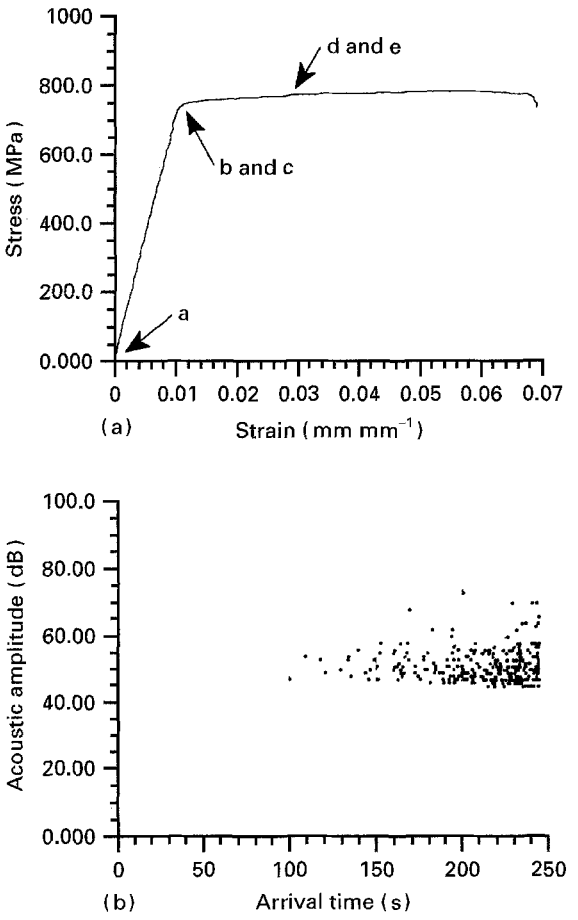

Figure 14 The extension dependence of the stress and the amplitude of AE of a specimen annealed at 1100 °C and cooled at a speed of 2 °C min^{-1}. The letters a–e along the stress–strain curve indicate the stress levels at which the respective micrographs in Fig. 15 were taken. (Strain rate: 2.9×10^{-4} s^{-1}.)

microstructural examination of these specimens revealed that microcracking had occurred near the yield strength, as shown in Fig. 15. The reason for the change in deformation mechanism is not well understood. However, the disappearance of AE near the yield strength is believed to be related to the microcracking. Factors favouring the detectability of AE due to microscopic fracture sources are high ambient stress, large crack radius and fast crack speed [15]. Thus, the microcracks observed must propagate slowly because no AE was detected. Another evidence for the stable propagation of these microcracks was a reasonably large elongation of 6% shown by four specimens with this processing condition. At the later stage of deformation, both microcracks and slip lines were easily observed (Fig. 15d and e). The appearance of detectable AE at this stage was most likely related to the operation of dislocation sources, as shown in Fig. 15d and e.

3.7. Second phase effect

The second phase, beta, in the present specimens existed in two morphologies: one was in an intergranular form and the other in plate form. In the former case, the grain boundaries of the alpha phase were effective barriers to dislocation motion. Thus, the presence of beta at the grain boundaries had little influence on the dislocation motion, and the presence of beta merely reduced the volume fraction of the alpha phase. In the latter case, dislocation motion in the alpha phase could not be interrupted by the presence of the beta phase, as suggested by the continuous slip lines within individual Widmanstatten colonies (Figs 12 and 15). The beta phase, which has a bcc crystal structure and a crystallographic relationship with the alpha plates, also deforms plastically and is too soft to be an effective barrier to dislocation motion [29]. As a result, AE in this case behaved as though there were no beta phase, i.e. it was again dominated by the deformation behaviour of the alpha phase.

The current observation agrees with other studies [30, 31]; these studies have shown that when the second phase precipitates are strong, widely spaced and

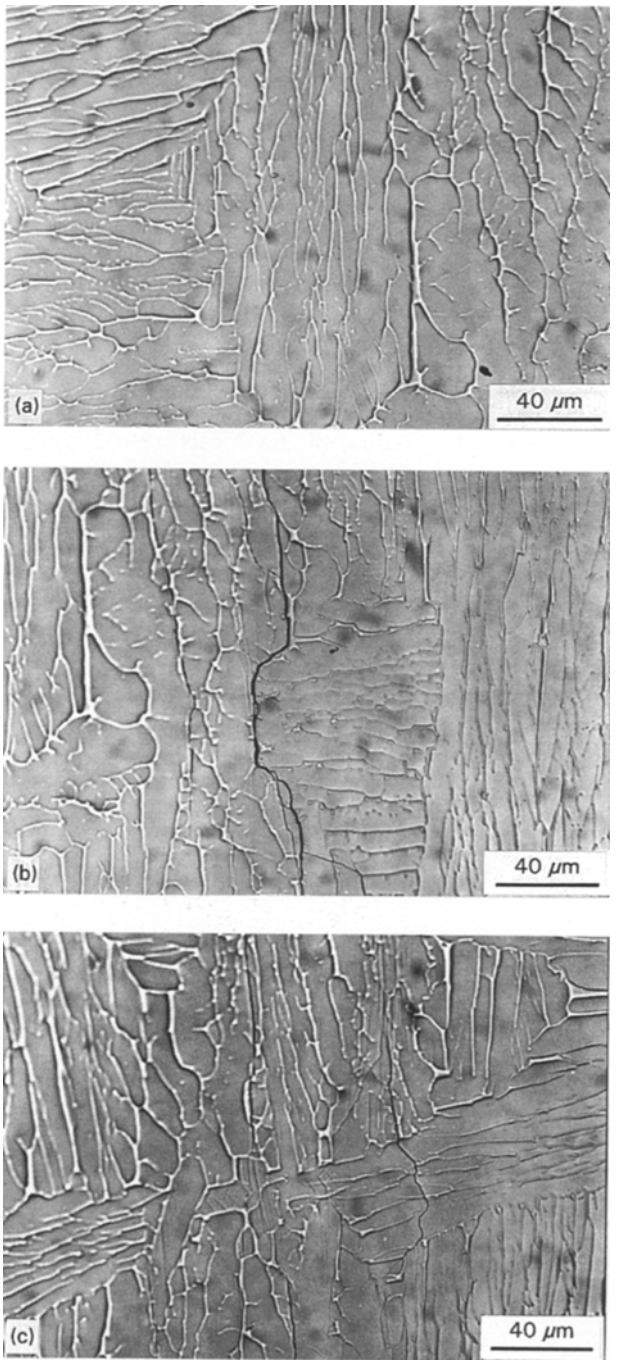

Fig. 15 (Continued)

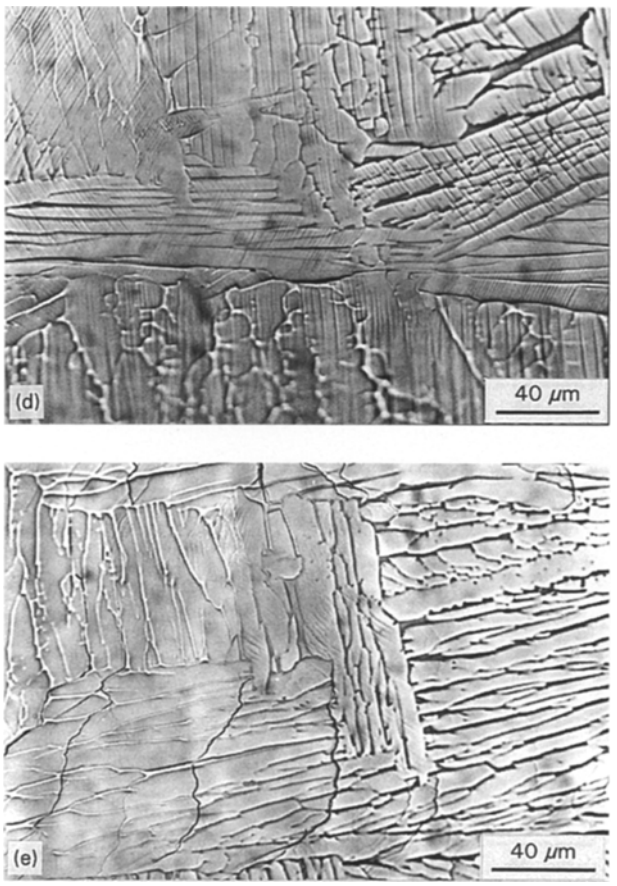

Figure 15 The microstructural change and microcracking during tensile deformation of a specimen annealed at 1100 °C and cooled at a speed of 2 °C min^{-1}. The stress levels at which the micrographs (a)–(e) were taken are shown in Fig. 14. Note that micrographs (b) and (c) were taken at the same stress level but at different areas, as were (d) and (e).

incoherent with the matrix, only moderate levels of AE are detected. However, when the second phase precipitates are weak, closely spaced and coherent with the matrix, dislocations may shear them, giving rise to intense AE. The beta plates in Widmanstatten colonies are weak and coherent with the alpha plates, and thus dislocations can shear them, producing detectable AE. Otherwise, the dislocation motion would have been limited within individual alpha phases, leading to a very small mean free path and AE with very low amplitudes.

Based on the above discussion, it can be concluded that a weak ductile phase embedded in another ductile phase in a small amount with a morphology of either an intergranular network or thin plates which are coherent with the matrix could have little influence on the AE of this two-phase material.

4. Conclusions

The AE of Ti–6Al–4V, a two-phase alloy, has been studied using an *in situ* microstructural observation technique coupled with mechanical deformation. Based on this study, the following conclusions related to the deformation and AE of Ti–6Al–4V can be offered.

1. The amplitude of AE events exhibits a maximum near the yield stress and decreases gradually as the material work hardens. This strain dependence of AE is attributed to the operation of Frank–Read sources and the decrease in the mean free path between sessile dislocations with the increase in work hardening.
2. An increasing strain rate increases the AE events amplitude and the rate of AE. The increase in the amplitude is related to an increase in the population of moving dislocations and/or the velocity of moving dislocations, while the increase of the rate of AE is attributed to a greater frequency of dislocation operation.
3. Increasing grain size results in: (a) an increase in the amplitude of AE events near the yield stress; (b) an increase in the total events of AE in each deformation test; and (c) a decrease in the rate of AE near the yield stress. These changes are due to the change in the largest radius the dislocations can expand.
4. Microvoid coalescence contributes to the sudden increase in the AE events and amplitude just before the final fracture of this material.
5. The beta phase exists in a morphology of either an intergranular network or thin plates. However, both of the morphologies exhibit little influence on the AE characteristics of this material because of the deformability of the beta phase.
6. Location analysis of AE sources suggests that a weak cross-section in Ti–6Al–4V is usually the location where yields first and initiates fracture.

Acknowledgements

One of the authors (LS) gratefully acknowledges the support from the Materials Directorate, Wright Laboratory, Wright–Patterson Air Force Base, Ohio, through a contract (F33615-90-C-5944) with Systran Corporation, with Mr Milton Zellmer as the contract manager.

References

1. J. G. BAKUCKAS JR, W. H. PROSSER and W. S. JOHNSON, "Monitoring damage growth in titanium matrix composites using acoustic emission" (NASA Technical Memorandum 107 742, 1993).
2. S. W. SCHWENKER, I. ROMAN and D. EYLON, in "Advanced composite '93", edited by T. Chandra and A. R. Dhingra (TMS, warrendale, PA, 1993) p. 1169.
3. R. B. PIPES, N. J. BALLINTYN, W. R. SCOTT and J. M. CARLYLE, in "Composite materials: testing and design" (ASTM STP 617, American Society for Testing and Materials, Philadelphia, 1976) p. 153.
4. M. S. MADHUKAR and J. AWERBUCH, in "Composite materials: testing and design", edited by J. M. Whitney (ASTM STP 893, American Society for Testing and Materials, Philadelphia, 1986) p. 337.
5. G. PEZZOTTI, K. NIIHARA and T. NISHIDA, *J. Testing and Evaluation*, **21** (1993) 358.
6. M. BOUQUET, J. M. BIRBIS and J. M. QUENISSET, *Compos. Sci. Technol.* **37** (1990) 223.
7. N. TAKEDA, O. CHEN, T. KISHI, W. TREDWAY and K. PREWO, *Engng. Fract. Mech.* **40** (1991) 791.
8. C. CANEVA, S. OLIVIERI, C. SANTULLI and G. BONIFAZI, *Compos. Struct.* **25** (1993) 121.
9. A. FUJITA, H. HAMADA and Z. MAEKAWA, *J. Compos. Mater.* **27** (1993) 1428.
10. M. WEVERS, I. VERPOEST, E. AERNOUDT and P. D. MEESTER, in "Acoustic emission", edited by J. Eisenblatter (DGM Informationsgesellschaft, Verlag, 1988) p. 59.

11. H. HANSMANN and H. G. MOSLÉ, in "Acoustic emission", edited by J. Eisenblatter (DGM Informationsgesellschaft, Verlag, 1988) p. 77.
12. P. RUNOW and E. JANOSCHEK, in "Acoustic emission", edited by J. Eisenblätter (DGM Informationsgesellschaft, Verlag, 1988) p. 93.
13. A. SIEGMANN and R. G. KANDER, *Polym. Compos.* **13** (1992) 108.
14. M. FAUDREE, E. BAER, A. HILTNER and J. COLLISTER, *J. Compos. Mater.* **22** (1988) 1170.
15. R. K. MILLER and P. MCINTIRE (Eds) "Nondestructive testing handbook, Vol. 5, Acoustic Emission Testing", (American Society for Nondestructive Testing, 1987).
16. J. R. FREDERICK and D. K. FELBECK, in "Acoustic emission", (ASTM STP 505, American Society for Testing and Materials, Philadelphia, 1972) p. 129.
17. D. ROUBY and P. FLEISCHMANN, *Phys. Stat. Sol. (a)* **48** (1978) 439.
18. R. C. BILL, J. R. FREDERICK and D. K. FELBECK, *J. Mater. Sci.* **14** (1979) 25.
19. C. B. SCRUBY, C. JONES, J. M. TITCHMARSH and H. N. G. WADLEY, *Metal Sci.* June (1981) 241.
20. C. SCRUBY, H. WADLEY and J. E. SINCLAIR, *Phil. Mag.* **44A** (1981) 249.
21. P. P. GILLS, in "Acoustic emission" (ASTM STP 505, American Society for Testing and Materials, Philadelphia, 1972) p. 20.
22. C. H. CACERES and H. R. BERTORELLO, *Scripta Metall.* **17** (1983) 1115.
23. F. ZEIDES and I. ROMAN, *Scripta Metall. Mater.* **24** (1990) 1919.
24. F. CHMELIK, Z. TROJANOVA, P. LUKAC and Z. PREVOROVSKY, *J. Mater. Sci. Lett.* **11** (1992) 91.
25. C. H. CACERES and A. H. RODRIGUEZ, *Acta Metall.* **35** (1987) 2851.
26. F. CHMELIK, Z. TROJANOVA, Z. PREVOROVSKY and P. LUKAC, *Mater. Sci. Engng.* **A164** (1993) 260.
27. P. FLEISCHMANN and D. ROUBY, in "Acoustic emission" (DGM Deutsche Gesellschaft Fur Metalljunde E. V., 1979) p. 39.
28. R. M. FISHER and J. S. LALLY, *Can. J. Phys.* **45** (1967) 1147.
29. K. S. CHAN, C. C. WOJCIK and D. A. KOSS, *Metall. Trans.* **12A** (1981) 1899.
30. K. L. RUSBRIDGE, C. B. SCRUBY and H. N. G. WADLEY, *Mater. Sci. Engng.* **59** (1983) 151.
31. C. B. SCRUBY, H. N. G. WADLEY and K. L. RUSBRIDGE, *ibid.* **59** (1983) 169.

Received 8 September 1994
and accepted 23 February 1995